ELSEVIER

Journal of Structural Geology 29 (2007) 396–410

JOURNAL OF STRUCTURAL GEOLOGY

www.elsevier.com/locate/jsg

Deflection and propagation of fluid-driven fractures at frictional bedding interfaces: A numerical investigation

Xi Zhang [a,*], Robert G. Jeffrey [a], Marc Thiercelin [b]

[a] *CSIRO Petroleum Resources, Bayview Avenue, Clayton, VIC 3168, Australia*
[b] *Schlumberger Moscow Research, 9 Taganskaya, Moscow, 109147, Russia*

Received 9 June 2006; received in revised form 12 September 2006; accepted 20 September 2006
Available online 14 November 2006

Abstract

Propagation of fluid-driven or hydraulic fractures deflected at bedding interfaces in layered sedimentary rocks and subsequent fluid invasion is investigated numerically using a two-dimensional boundary element model. The fracture is driven by an incompressible Newtonian fluid injected at a constant rate. The frictional stress on the interface is assumed to obey Coulomb's frictional law without cohesion. The bedding interface can be given a non-zero minimum fluid conductivity. A numerical scheme that deals with both rock deformation and fluid flow is presented and its accuracy is verified in terms of comparisons with existing results. To explore the mechanisms involved in fluid and fracture invasion into the interface, parametric studies are carried out for different elastic modulus contrasts, in situ stresses, interfacial frictional coefficients, distances from the injection point to the interface, and fluid viscosities. The results are provided as time-dependent variations of displacements, fluid pressures, contact stresses and fluid fronts. Fracture deflection and fluid invasion into the interface are found to rely essentially on local stress and deformation states at the intersection point. Fluid invasion and fracture growth may be delayed or inhibited when the interface is subjected to large confining stress or when fluid viscosity is relatively low for cases where the fluid-driven fracture originates in the softer layer. In this case, a greater layer-parallel tensile stress is produced and can lead to fracture propagation through the bedding contact. Low to medium frictional strength is found to promote fluid penetration and T-shaped fracture formation by interfacial opening. If the hydraulic fracture originates in a stiffer layer, fluid invasion into bedding contacts can occur smoothly without the occurrence of interface closure, and the fracture is thus terminated by forming a T-shaped fracture at the bedding interface. For fracture deflection into and growth along the interface in the absence of interface closure, the long-time responses resemble the solution for a fluid-driven fracture growing along a frictionless interface with vanishing toughness.

Keywords: Fluid-driven fracture; Frictional bedding interface; Fracture deflection; Fluid invasion; Numerical modelling

1. Introduction

Opening-mode fractures driven by fluids such as water and magma which are called fluid-driven fractures or hydraulic fractures have been observed to play a role in many geologic processes. Magma-driven volcanic dikes and hazards associated with them have motivated geologists and geophysicists to develop models to aid the studies of their behaviour (Rubin, 1995). The fracturing of rock formations by pressurized fluid is also a common method applied to stimulation of oil and gas wells in a variety of reservoir rocks (Warpinski and Teufel, 1987; Daneshy, 2003). Over the past years, a number of less-conventional uses of hydraulic fracturing technology, often resulting in more complex fracture geometries, have been introduced, among them, stimulation of geothermal reservoirs (Pine and Batchelor, 1984), stimulation of fractured shale and coalbed methane reservoirs, inducing caving in coal and metal mining (Van As and Jeffrey, 2000), and disposing of waste by injection into underground rock formations (Moschovidis et al., 1994).

* Corresponding author. +61 3 95458388; fax: +61 3 95458380.
E-mail address: xi.zhang@csiro.au (X. Zhang).

0191-8141/$ - see front matter © 2006 Elsevier Ltd. All rights reserved.
doi:10.1016/j.jsg.2006.09.013

A considerable number of laboratory and field studies of various kinds have demonstrated that branched and non-planar fracture growth is not only possible but fairly common (Warpinski and Teufel, 1987; Price and Cosgrove, 1990; Jeffrey, 1996). Geological discontinuities such as natural joints, faults and flaws, as well as bedding planes, in hydrocarbon reservoir rocks and in ore bodies (Warpinski and Teufel, 1987; Pollard and Aydin, 1988, among others), may contribute to the branching of hydraulic fractures. The bedding planes in layered sedimentary rocks affect hydraulic fracture growth because of changes in rock properties and in situ stresses associated with the layers, as well as the effect their frictional response has on fracture growth. For example, sharp changes in direction of a dike into an existing plane of weakness or parting plane can be found along the trace of dike intrusions (Price and Cosgrove, 1990). Furthermore, similar offsets in fracture pathways have been documented in man-made hydraulic fractures that have been mined and mapped (van As and Jeffrey, 2000; Warpinski and Teufel, 1987; Jeffrey et al., 1995). Because imperfectly bonded layer interfaces interact with and modify the propagation pathways of hydraulic fractures (Baer, 1991; Helgeson and Aydin, 1991; Narr and Suppe, 1991; Gross, 1993; Fischer et al., 1995; Becker and Gross, 1996; Cooke and Underwood, 2001), a model for the intersecting process must include the properties of interface and fracturing fluid.

In general, there are four types of interaction between a fluid-driven fracture and a bedding contact within layered sedimentary rocks, as sketched in Fig. 1. Fractures can penetrate through the bedding contacts without any division of the fracture path and the vertical fluid flow. This type of crossing is what is implicitly assumed to occur by all current hydraulic fracture design models. In the opposite extreme case, the hydraulic fracture may be arrested or blunted at the bedding contact due to large slip along the contact. Between these above two extremes, a potential intermediate state is that the fracture and the fluid flow are deflected into the bedding plane and are divided into two branches. If the interface is free of flaws, the fluid will invade it in the same way as an opening-mode hydraulic fracture growing along the horizontal bedding plane, so that the vertical fracture eventually terminates at the bedding plane, becoming a T-shaped fracture. Moreover, if there are flaws on the interface, potential re-initiation of a new fracture from one flaw will leave a step-over at the bedding interface (Pollard and Aydin, 1988; Cooke and Underwood, 2001).

Most previous investigations, such as the studies by Baer (1991), Helgeson and Aydin (1991) and Narr and Suppe (1991), among others, have focused on fracture behaviours within strata. Based on the elasticity considerations applied to perfectly bonded interfaces or strong interfaces, a fracture initiated in the stiffer of the two layers is able to advance towards and enter into the softer layer, but is not able to grow from soft to stiff. For strong interfaces, the elastic solutions for a crossing fracture can be found in the work by Erdogan and Biricikoglu (1973). However, the assumption of strong interfaces is often incorrect for geological interfaces since most interfaces have limited shear strength. For an interface that has a finite frictional strength described by the Coulomb criterion, the shear stress that can be carried by the interface or bedding plane is limited (Jaeger and Cook, 1979), and frictional sliding can take place. Fracture–interface interaction with frictional sliding, but without opening along the interface, was studied theoretically by Weertman (1980), Keer and Chen (1981) and Lam and Cleary (1984). In these studies, the distribution of the frictional stresses along the interface was assumed ad hoc. This assumed distribution of shear stress limits the application of their results. In addition, interface crossing can induce not only slip, but also opening at weak bedding contacts (Jeffrey et al., 1987; Dyer, 1988; Fischer et al., 1995; Cooke and Underwood, 2001; Gudmundsson and Brenner, 2001).

For fluid-driven fracture growth, interfacial opening can arise from fluid penetration. The build-up of fluid pressure on the bedding contact can open the interface, and this in turn facilitates further fluid penetration. Fig. 2 shows a hydraulic fracture propped with sand that was mapped after mining. The fracture was vertical in the coal seam and also grew horizontally along the interface between the coal and the overlying rock (Jeffrey et al., 1994) to form a T-shaped fracture shape. Of course, the growth of fluid-driven fractures along bedding planes as shown in Figs. 1 and 2 will alter fracture growth and fluid flow paths in all directions, and will affect the overall fracture behaviour. Branching of fluid-driven fractures into interfaces has an obvious and significant effect on

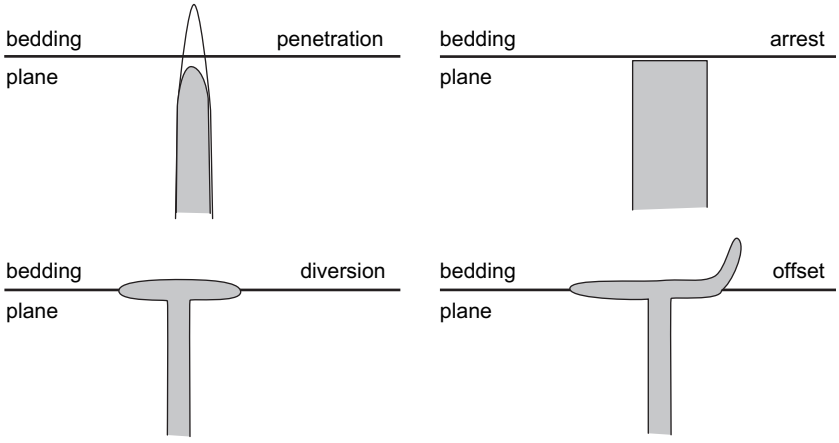

Fig. 1. Four types of interaction between hydraulic fractures and bedding planes (Thiercelin et al., 1987).

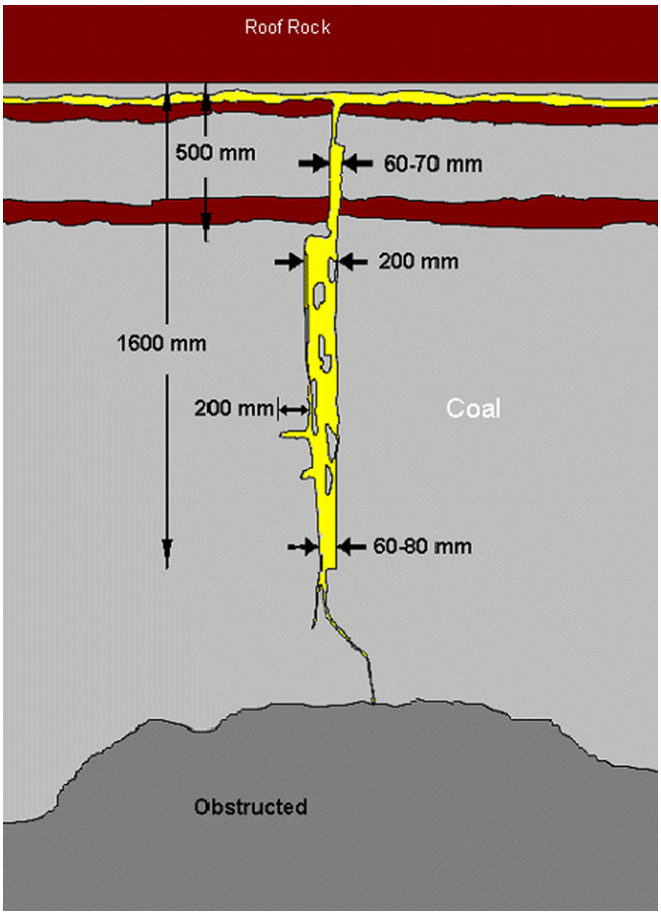

Fig. 2. A sand-propped hydraulic fracture that grew vertically in a coal seam and horizontally along the interface between the coal and the roof rock (Jeffrey et al., 1994).

fracture geometry, but has not yet been included in the studies of hydraulic fracture processes, to the authors' knowledge. In this paper, we will use numerical experiments to investigate the potential mechanisms of hydraulic fracture deflection and propagation and subsequent fluid invasion at a frictional bedding interface. The fracture will not be allowed to penetrate into the adjacent layer or to induce new fracture in it at some location along the interface. Branching of the hydraulic fracture which is initially perpendicular to the bedding contact is controlled by many parameters such as (1) frictional coefficient of the interface, (2) elastic properties of the layers, (3) remote stress conditions and (4) injected fluid viscosity. The injection rate is held as a constant for all cases, although it can affect the fracture deflection, too. Numerical results based on a two-dimensional boundary element model will be presented to address the effects of these factors on the propagation process of fluid-driven fractures.

2. Problem formulation

The natural system we are modelling is a bedded sedimentary rock containing a single fluid-driven fracture confined to one layer, as shown in Fig. 3. The hydraulic fracture intersects

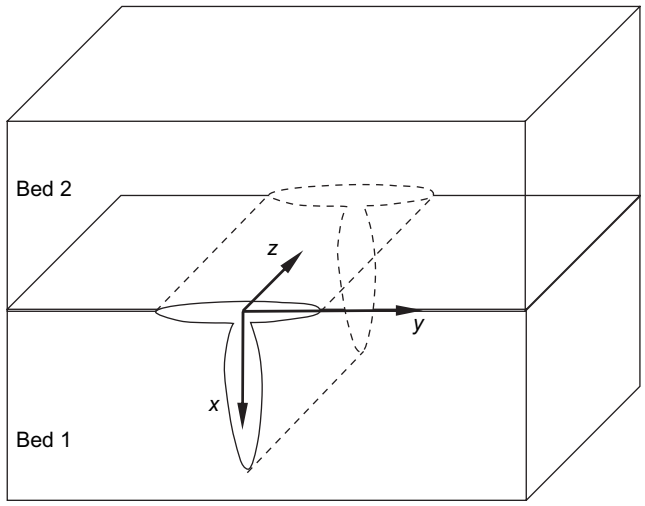

Fig. 3. Schematic geometry of a fluid-driven fracture deflecting at a bedding plane.

and then deflects into the bedding plane. This T-shape fracture is assumed to be infinitely long in the z-direction. This fracture geometry is similar to the intersection of a PKN-like (blade-like) fluid-driven fracture with a bedding plane. Alternatively, if the leading edge of a large three-dimensional fracture has a very small curvature, its coalescence with a bedding plane is represented approximately by such a two-dimensional model. If the T-shaped fracture develops as shown in Fig. 3, the two-dimensional model accurately represents plane-strain fracture behaviour on an $x-y$ cross-section.

Consider, as shown in Fig. 4, a plane-strain fracture propagating towards the interface between two linear-elastic half-planes. The infinite horizontal interface represents a bedding plane. However, we model the frictional interface as a very long fracture lying on the interface with frictional properties. The y-axis is taken to be parallel to the interface and the Cartesian coordinate system is depicted in Fig. 4. The origin of the

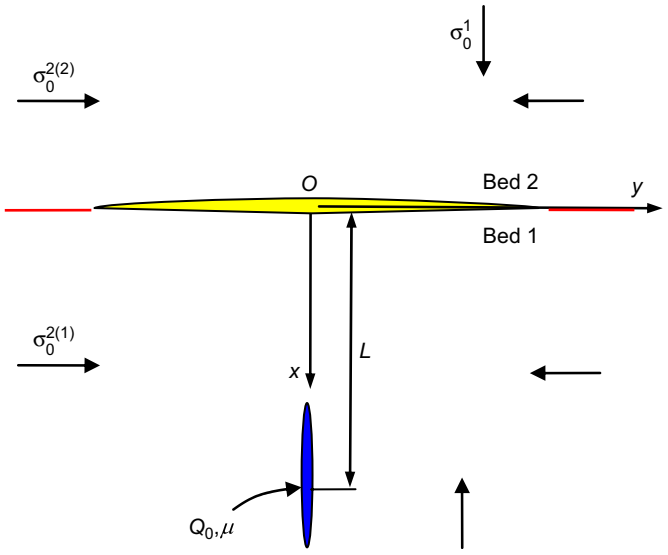

Fig. 4. Configuration used to examine intersection and deflection of a fluid-driven fracture at a frictional interface illustrating the definitions of various quantities to be used.

coordinate system is at the potential intersecting point between a vertical fluid-driven fracture and a bedding plane. The injection point is at a distance L away from the intersecting point. It is assumed that the rocks are impermeable, isotropic and elastic media. The Young's moduli, Poisson's ratios and fracture toughness for the rock layers are, respectively, E_i, ν_i and K_i^{C}, where subscript i denotes the layer $i = 1, 2$. A Newtonian fluid with viscosity μ is injected at a constant rate Q_0 into the vertical fracture. The vertical far-field stress is denoted by σ_0^1, and the layer-parallel far-field stresses in the upper and lower half-planes are $\sigma_0^{2(1)}$ and $\sigma_0^{2(2)}$, respectively. Fluid pressure and far-field stresses are taken as positive if in compression.

An equation, based on elasticity, provides the relationship between the normal, w, and shear, v, displacement discontinuities (DDs) of the fracture walls and the fluid pressure p_{f} inside the fracture. The formulation used is based upon a superposition scheme of singular dislocation dipole solutions. The fracture branches are numbered based on the tips, that is, there are N fractures if there are N tips. Summing up the contributions to the stresses from each fracture, the elasticity equation for equilibrium fractures in the framework of a Cartesian coordinate system is

$$\begin{aligned}\sigma_{\mathrm{n}}(\boldsymbol{x},t)-\sigma_1(\boldsymbol{x}) &= \sum_{r=1}^{N}\int_0^{\ell_r}[G_{11}(\boldsymbol{x},s,\alpha,\beta)w(s)\\ &\quad + G_{12}(\boldsymbol{x},s,\alpha,\beta)v(s)]\mathrm{d}s\\ \tau_{\mathrm{s}}(\boldsymbol{x},t)-\tau_1(\boldsymbol{x}) &= \sum_{r=1}^{N}\int_0^{\ell_r}[G_{21}(\boldsymbol{x},s,\alpha,\beta)w(s)\\ &\quad + G_{22}(\boldsymbol{x},s,\alpha,\beta)v(s)]\mathrm{d}s\end{aligned} \tag{1}$$

where $\boldsymbol{x} = (x, y)$ and t is time; $\mathrm{d}s$ is the infinitesimal arc length along the fracture; ℓ_r is the fracture length with a subscript index r identifying the fracture branch. σ_{n} is the normal stress and within the fluid-filled parts, it is equal to p_{f} and τ_{s} is the shear stress associated with the frictional sliding along the interface. σ_1 and τ_1 are the normal and shear stresses along the fracture direction at location $\boldsymbol{x}$ caused by the far-field stresses, respectively. G_{11}, G_{12}, G_{21}, G_{22} are hypersingular Green's functions whose expressions can be found in Zhang and Jeffrey (2006a). These Green's functions are dependent on the Dundurs' parameters, defined by

$$\alpha = \frac{\mu_2(\kappa_1+1)-\mu_1(\kappa_2+1)}{\mu_2(\kappa_1+1)+\mu_1(\kappa_2+1)};\quad \beta = \frac{\mu_2(\kappa_1-1)-\mu_1(\kappa_2-1)}{\mu_2(\kappa_1+1)+\mu_1(\kappa_2+1)} \tag{2}$$

where $\kappa_i = 3 - 4\nu_i$. The fracture index r will not be shown in the following equations.

In order to maintain continuity of strain across the interface, $\sigma_0^{2(1)}$ and $\sigma_0^{2(2)}$ are related by:

$$\frac{\sigma_0^{2(2)}}{\sigma_0^{2(1)}} = \frac{E_2(1-\nu_2)}{E_1(1-\nu_1)} + \left(\nu_2 - \frac{E_2(1-\nu_2)}{E_1(1-\nu_1)}\nu_1\right)\frac{\sigma_0^1}{\sigma_0^{2(1)}} \tag{3}$$

The fluid flow in the fractures is governed by the lubrication equation, that is, (Batchelor, 1967)

$$\frac{\partial w}{\partial t} = \frac{\partial}{\partial s}\left(\frac{w^3}{\mu'}\frac{\partial p_{\mathrm{f}}}{\partial s}\right) \tag{4}$$

where $\mu' = 12\mu$. Because we assume no fluid loss occurs into the impermeable rock, the global mass balance leads to:

$$\sum\int_0^{\ell_{\mathrm{f}}} w\mathrm{d}s = Q_0 t \tag{5}$$

where ℓ_{f} is the length of each fracture filled by fluid. The formulation allows for a fluid lag which is the distance between the fluid front ℓ_{f} and the fracture tip ℓ for each fracture branch. The fluid front can be found in terms of the flux $q(\ell_{\mathrm{f}})$ and the opening $w(\ell_{\mathrm{f}})$ at the fluid front in the form of

$$\dot{\ell}_{\mathrm{f}} = \frac{q(\ell_{\mathrm{f}})}{w(\ell_{\mathrm{f}})} \tag{6}$$

where the flux is defined as $q = (w^3/\mu')/(\partial p_{\mathrm{f}}/\partial s)$ based on Poiseuille's law.

At the injection point, the fluid flux is equal to the injection rate, that is,

$$q(0) = Q_0 \tag{7}$$

At the fracture tip, the opening and shearing DDs vanish, that is,

$$w(l) = v(l) = 0 \tag{8}$$

Generally speaking, bedding planes may have some roughness, minor and major offsets, and occasional curves and kinks associated with gouges and minerals, which often lower the shear strength (Pollard and Aydin, 1988). The frictional contact stresses on the rough interface must be taken into account in exploring the interactions between fluid-driven fractures and bedding planes. The Coulomb frictional law adopted in the numerical model provides a proportional relation between the frictional strength τ_{f} and the normal effective compressive stress, σ_{n}, that is,

$$|\tau_{\mathrm{f}}| = \lambda\sigma_{\mathrm{n}} \tag{9}$$

where λ is the frictional coefficient.

If the shear stress acting is less than the frictional strength, the fracture surface is in sticking mode, otherwise it is in sliding mode. The direction of sliding can be reversed when the tangential shear stress changes sign. The frictional stress and the shear DD increments should meet the following condition for the contact sliding mode (Tuhkuri, 1997)

$$\tau_{\mathrm{s}}\Delta v \le 0 \tag{10}$$

where Δv is the sliding increment.

In order to work out correct frictional modes for all contacts along the interface, an initial guess is used and a check is made

to ensure that the guess is correct at each time increment. If not, the contact and sliding modes are updated based upon the calculated stresses and displacements. The sticking or sliding condition is then applied and stresses and displacements are resolved followed by another check and modification until the contact modes converge at each location.

The fracture growth prior to intersection is based on the toughness in bed 1. Thus, we have

$$K_1^{\mathrm{I}} = K_1^{\mathrm{C}} \tag{11}$$

where K_1^{I} is the Mode I stress intensity factor.

Although the bedding planes are idealized as closed, smooth and continuous, they may be filled with minerals and gouges, or proppants in the case of previously placed hydraulic fractures. Any associated initial apertures will provide a hydraulic conductivity for fluid flow. The bedding plane can be assigned a minimum conductivity $w_{\mathrm{o}}^{\mathrm{h}}$ which is not a physical opening and does not affect stresses, but is only used in the fluid flow calculations.

As for fracture intersection of an interface, it is assumed that intersection occurs when the fracture tip is located within a small distance from the interface. For most cases, the interface is opened by interaction prior to intersection. The numerical treatment of fracture–interface intersection is outlined in the next section.

For T-shaped fractures formed post intersection (Fig. 5), fluid can invade into two fracture branches after intersection. The influx of each fracture branch must be calculated explicitly. A balance of flux into and out of the junction is prescribed, and the same fluid pressure is imposed on all fracture branches that meet at the junction. The outflow flux can be obtained by the volume changes in the vertical fracture at a given time step and this flux is initially divided into the two fracture branches according to the ratio of their conductivity. For the sake of finding the correct influx for each branch, the solution is then sought numerically by iterations so as to satisfy the conditions on flux balance and pressure continuity at the T-junction.

3. Numerical method

A numerical method with an implicit scheme for fracture opening and an explicit scheme for time is used to solve the boundary-value problem described by Eqs. (1) and (4)–(11). A similar procedure has been described by Zhang et al. (2002) for penny-shaped fracture growth in semi-infinite zero-toughness materials without fluid lag. Let T be an arbitrary time scale which can be defined as follows:

$$T = \frac{E'^2\mu'}{\left(\sigma_0^2\right)^3} \tag{12}$$

where $E' = E_1/(1-\nu_1^2)$.

Introduce a small parameter ε and a length scale $\overline{L}$ as follows:

$$\varepsilon = \left(\frac{\mu'}{E'T}\right)^{1/3}$$

$$\overline{L} = \left(\frac{E'Q_0^3T^4}{\mu'}\right)^{1/6} \tag{13}$$

and a dimensionless time and coordinates as follows:

$$\tau = \frac{t}{T} \quad \text{and} \quad \varsigma = (\xi,\eta) = \left(\frac{x_1}{\overline{L}}, \frac{x_2}{\overline{L}}\right) \tag{14}$$

Therefore, we can define the dimensionless fracture length, the size of the fluid-filled region, the opening and sliding DDs, as well as the normal and frictional stresses, as follows (Detournay, 2004):

$$\begin{aligned}
\ell &= \overline{L}\gamma(\tau)\\
\ell_{\mathrm{f}} &= \overline{L}\varphi(\tau)\\
w &= \varepsilon\overline{L}\Omega(\xi,\eta;\tau)\\
v &= \varepsilon\overline{L}\Theta(\xi,\eta;\tau)\\
\sigma_{\mathrm{n}} &= \varepsilon E'\Pi(\xi,\eta;\tau)\\
\tau_{\mathrm{f}} &= \varepsilon E'\Phi(\xi,\eta;\tau)
\end{aligned} \tag{15}$$

Based on Eq. (15), Eqs. (1) and (4)–(11) can be rewritten as follows:

$$\begin{aligned}
\Pi(\varsigma,\tau) - \Pi_1(\varsigma) = \sum \int_0^{\gamma} [&\Im_{11}(\varsigma,\chi,\alpha,\beta)\Omega(\chi,\tau)\\
&+ \Im_{12}(\varsigma,\chi,\alpha,\beta)\Theta(\chi,\tau)]\mathrm{d}\chi\\
\Phi(\varsigma,\tau) - \Phi_1(\varsigma) = \sum \int_0^{\gamma} [&\Im_{21}(\varsigma,\chi,\alpha,\beta)\Omega(\chi,\tau)\\
&+ \Im_{22}(\varsigma,\chi,\alpha,\beta)\Theta(\chi,\tau)]\mathrm{d}\chi
\end{aligned} \tag{16}$$

$$\frac{\partial\Omega}{\partial\tau} = \frac{\partial}{\partial\chi}\left(\Omega^3\frac{\partial\Pi_{\mathrm{f}}}{\partial\chi}\right) \tag{17}$$

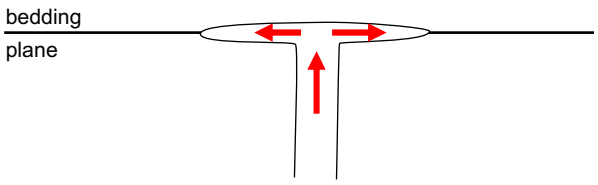

Fig. 5. Configuration at a T-junction and stress and fluid conditions at the intersection.

$$\sum \int_0^{\varphi} \Omega \, \mathrm{d}\chi = \tau \tag{18}$$

$$\dot{\varphi} = \frac{\Psi(\varphi)}{\Omega(\varphi)} \tag{19}$$

$$\Psi(0) = 1 \tag{20}$$

$$\Omega(\gamma) = \Theta(\gamma) = 0 \tag{21}$$

$$|\Phi| \leq \lambda \Pi \tag{22}$$

$$\kappa_1^{\mathrm{I}} = \kappa_1^{\mathrm{C}} \tag{23}$$

where $\mathrm{d}\chi = \sqrt{\mathrm{d}\xi^2 + \mathrm{d}\eta^2}$ is the infinitesimal segment length; Π_1, Φ_1 are defined by the relations $\sigma_1(\boldsymbol{x}) = \varepsilon E' \Pi_1(\varsigma)$ and $\tau_1(\boldsymbol{x}) = \varepsilon E' \Phi_1(\varsigma)$; Π_{f} is defined by $p_{\mathrm{f}} = \varepsilon E' \Pi_{\mathrm{f}}$; $\Psi = \Omega^3 \partial \Pi_{\mathrm{f}} / \partial \chi$; $\Im_{ij}$ are the Green's functions in the normalized coordinate system;

$$\kappa_1^{\mathrm{I}} = 4\left(\frac{2}{\pi}\right)^{1/2} \frac{K_1^{\mathrm{I}}}{\left(E'^3 \mu' Q_0\right)^{1/4}} \quad \kappa_1^{\mathrm{C}} = 4\left(\frac{2}{\pi}\right)^{1/2} \frac{K_1^{\mathrm{C}}}{\left(E'^3 \mu' Q_0\right)^{1/4}} \tag{24}$$

A discretised form of the above equations with associated boundary conditions can be obtained in the same manner as used in Zhang et al. (2002). Numerical solutions are based on a fixed element size $\Delta\eta$ and a small, but adjustable time step, $\Delta\tau$. The current element number for a fracture at an elapsed time is denoted by M and the corresponding element number fully occupied by fluid is m. For the elasticity equations, we use the DD method with constant strength for each element (Crouch and Starfield, 1990). Only discretisation along the fracture is required. The lubrication equation can be solved at a time increment $\Delta\tau$ by means of the Finite Difference Method (FDM). When the propagation criterion is met, a fixed size $\Delta\eta$ equal to the standard element size, is added to the fracture tip in the propagation direction. To improve the accuracy of the stress intensity factor calculation, a mesh adaptive scheme is employed by using six fine elements close to the fracture tip. These elements are one-third in size of the standard sized elements. When a fracture grows, the mesh is adjusted so that only six fine elements are used. The traction and opening must be mapped to the new mesh after each growth step. In addition, at the fracture tip, a singular element (square root shape function) is used.

The length ratio of the fluid length and the element size in the partially filled element $m+1$ is denoted by δ. The fracture length is $\gamma = M\Delta\eta$ and the fluid front is at $\varphi = (m+\delta)\Delta\eta$. If the filling element is one of the finer elements, $\Delta\eta$ is replaced by $\Delta\eta/3$. The flux into the filling element can be obtained by the equation of mass continuity (Zhang et al., 2005). In particular, the increment of δ for a time step $\Delta\tau$ can be expressed as follows:

$$\Delta\delta = \frac{\Psi_{m+1}}{\Omega_{m+1}} \Delta\tau \tag{25}$$

The coalescence between a hydraulic fracture and an interface is treated by the following numerical scheme. Linkage is assumed to occur when the interface is approached to within a radius of one standard element size $\Delta\eta$ from the tip of hydraulic fracture. In Fig. 6(a), point E is the projected intersection point based on the direction determined from the maximum hoop tensile stress. Although the two fractures may connect in a curved or even zigzag path, the linking elements are treated as straight, as shown in Fig. 6(b). The final linkage is made from the hydraulic fracture tip to the nearest end point of the elements on the joint. Before the fracture linkage starts, mesh refinement is carried out. The size used for the connecting elements is less than or equal to $\Delta\eta/3$ so as to reduce the error caused by this smoothing process to an acceptable level. In the algorithm, two elements on the interface closest to the intersecting point E can be identified and each of these two elements is divided into three equal-size elements, as shown in Fig. 6(b). The linkage point is then selected as the end point F of one of these fine elements that is the closest to the proposed intersecting point E.

3.1. Error assessment

To test the model accuracy in the calculation of stresses and DDs, a static fracture intersecting two layers is revisited here. The fracture configuration is illustrated in Fig. 7. The elastic constants and fracture sizes are exactly the same as those used by Erdogan and Biricikoglu (1973) and Peirce and Siebrits (2001). There is no vertical far-field stress and the horizontal remote stresses for the two layers are related according to Eq. (3), that is,

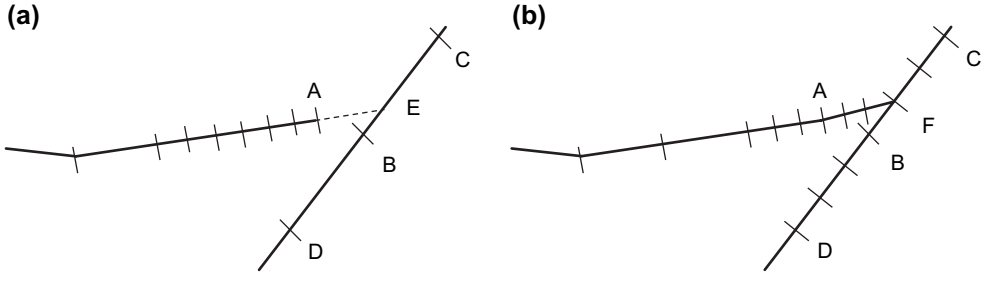

Fig. 6. Schematic of fracture coalescence process. (a) Prior to coalescence and (b) post coalescence.

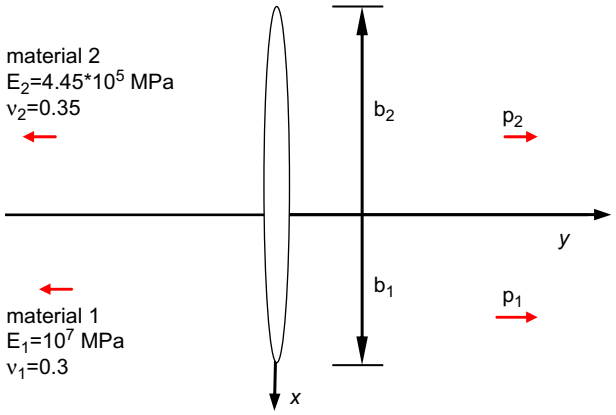

Fig. 7. Pressurized fracture crossing a bimaterial interface.

$$\frac{1-\nu_1^2}{E_1}p_1 = \frac{1-\nu_2^2}{E_2}p_2 \tag{26}$$

In Table 1, we provide the stress intensity factors for the two fracture tips, determined by our model, by MLAYER2D (Peirce and Siebrits, 2001) and by the semi-analytic solution (Erdogan and Biricikoglu, 1973), respectively. Our results were obtained using 100 elements. A good agreement is observed among these results. Our numerical approximations are within 1% of both the semi-analytical solutions and the MLAYER2D results.

To check the applicability of the model to interfacial fracture problems, an interfacial fracture with a length $2a$, which is subjected to a uniform remote tension p, is examined numerically. For the case of $\alpha = 0.8$ and $\beta = \alpha/4$, the numerical results of opening and sliding profiles are depicted in Fig. 8. The corresponding analytical solutions are given by Hutchinson et al. (1987)

$$w + iv = \frac{p\sqrt{a^2-x^2}}{C\sqrt{1-\beta^2}}\left|\frac{x+a}{x-a}\right|^{i\varepsilon} \tag{27}$$

where C is the effective bimaterial modulus and ε the bimaterial constant. Both of them are defined, respectively, by,

$$C = \frac{2\mu_1(1+\alpha)}{(\kappa_1+1)(1-\beta^2)} = \frac{2\mu_{21}(1-\alpha)}{(\kappa_2+1)(1-\beta^2)} \quad \text{and}$$
$$\varepsilon = \frac{1}{2\pi}\ln\left(\frac{1-\beta}{1+\beta}\right) \tag{28}$$

Table 1
Stress intensity factors for three different models

b_2/b_1	Fracture tip normalized stress intensity	This paper	MLAYER2D (Peirce and Siebrits, 2001)	Erdogan and Biricikoglu (1973)
0.05	$K_I(b_1)/(p_1\sqrt{l})$	1.4055	1.4035	1.4067
	$K_I(b_2)/(p_2\sqrt{l})$	4.2780	4.2268	4.3607
1.00	$K_I(b_1)/(p_1\sqrt{l})$	1.0918	1.0921	1.0931
	$K_I(b_2)/(p_2\sqrt{l})$	1.1571	1.1586	1.1787
2.00	$K_I(b_1)/(p_1\sqrt{l})$	0.9118	0.9124	0.9129
	$K_I(b_2)/(p_2\sqrt{l})$	0.9654	0.9676	0.9770

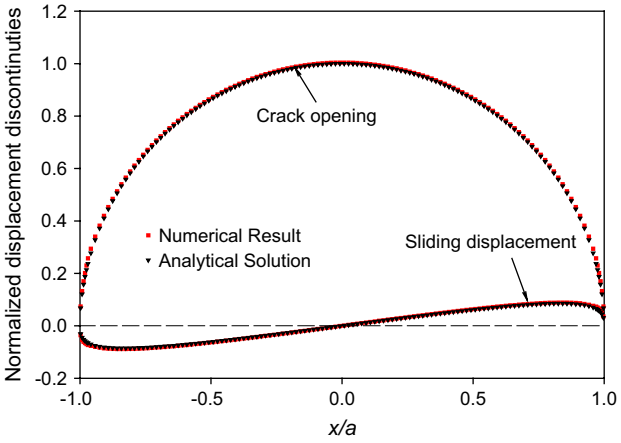

Fig. 8. Fracture opening and sliding DDs for an interface fracture at $\alpha = 0.8$ and $\beta = \alpha/4$.

In Fig. 8, the fracture opening and sliding DDs are normalized by $pa/C\sqrt{1-\beta^2}$. A good agreement between the numerical result and the analytical solution is found. These relatively small discrepancies indicate the numerical model proposed here is acceptable for fracture problems in bi-material layered rocks.

4. Numerical results

To investigate the effects of slip and debonding of bedding interfaces on hydraulic fracture crossing interactions, numerical experiments are performed based on the configuration shown in Fig. 4. For the sake of simplicity, the long frictional bedding plane is given an interface toughness of zero and growth of the hydraulic fracture in the direction away from the interface is arbitrarily prevented. Plane-strain fracture growth is studied under a remote stress field with the vertical compressive stress σ_0^1 as a parameter, while the horizontal compressive stress in rock 1 is specified as $\sigma_0^{2(1)} = 4$ MPa and its counterpart in rock 2 is determined by Eq. (3). One of the two layers has Young's modulus $E = 3300$ MPa and Poisson's ratio $\nu = 0.4$ and the other has $E = 10\,000$ MPa and Poisson's ratio $\nu = 0.4$. If the fluid-driven fracture grows from the soft to the stiff layer, $\alpha = 0.504$ and $\beta = 0.084$, and if from the stiff to the soft layer, $\alpha = -0.504$ and $\beta = -0.084$. The fracture toughness of both rocks is given as $K_I^C = 0.5$ MPa m$^{1/2}$. The injection rate is fixed as $Q_0 = 0.006$ m^2/s and the dynamic fluid viscosity varies as $\mu = 0.001$, 0.01, 0.1 Pa s. The frictional coefficient of the bedding interface varies as 0.1, 0.5 and 1.0. In addition, there is a minimum hydraulic conductivity (w_o^h) along the bedding interface, although it does not affect the stress fields. In the calculation, $w_o^h = 0.1$ mm is chosen for all cases.

To investigate fluid invasion due to fracture termination at the frictional bedding contacts, we track the fluid pressure at the borehole and at the intersecting point so as to deduce the possible fluid patterns for various material parameters and geometric arrangements. Since the geometric symmetry holds for two branched daughter fractures as shown in Fig. 9, we can define the distance s to the borehole along the fracture

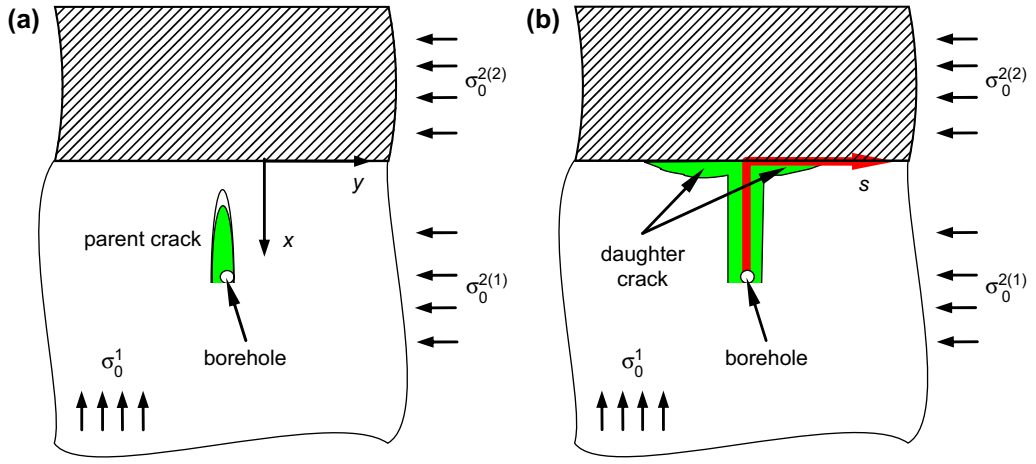

Fig. 9. Geometry used in elastic analysis of fracture growth along the interface. The fracture geometry is symmetric with respect to the line of the parent fluid-driven fracture. s denotes the distance to the injection well along the fracture path. (a) Prior to intersection and (b) post intersection.

pathways as a new coordinate to facilitate presenting results. To determine how rapid the fluid invades the interface, the stress and opening profiles at the same elapsed time are compared. For numerical experiments, there are two different material arrangements depending on which bed the parent hydraulic fracture is located in. Let us begin with the cases where the injection point is in the softer layer.

4.1. Soft to stiff

In Fig. 10, the time dependence of injection pressures is given for different distances L in the case of $\mu = 0.1$ Pa s, $\sigma_0^1 = 5$ MPa and $\lambda = 1.0$. The "vertical fracture" solution is presented for the growth of the parent fracture in the softer layer without an interface. In the calculation, after coalescence of the parent hydraulic fracture and the interface, the fluid front advance is impeded by the interface. The injection pressure then starts to increase so as to force the fluid into the interface, although it keeps decreasing in the "vertical fracture" solution. There is a peak of fluid pressure for each curve in Fig. 10 required to overcome the stress barrier imposed by the compressive stress across the interface which arises from both the far-field stresses and the additional stress induced on the interface by the fluid pressure in the parent fracture. Fluid and fracture invasion becomes easier after these peaks. It is noted that as L increases, the pressure difference between the value at intersection and the peak decreases, but the time interval for this pressure change increases. In addition, after a certain period for fluid invasion into the interface, the injection pressure decreases to the plateau value. The closer the borehole is to the intersecting point, the larger is the plateau value of the injection pressure. In contrast, the injection pressure decreases continuously with time for the "vertical fracture" solution. The differences between the curves and the "vertical fracture" solution arise from the change in fracture geometry, modulus contrast and far-field stresses. The higher plateau value of injection pressure at $L = 1$ m implies a stronger mechanical interaction around the T-junction for a short parent fracture. However, for uniformly pressurised fractures, large parent fracture lengths are associated with an increase in stress concentration across the interface (Lawn, 1993).

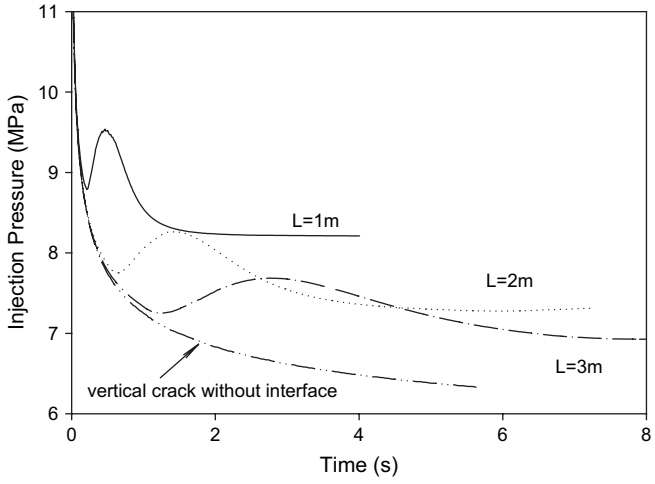

Fig. 10. Injection pressure versus time curves for various distances in the case of $\mu = 0.1$ Pa s, $\sigma_0^1 = 5$ MPa and $\lambda = 1.0$.

Fluid pressure at the intersecting point first increases with time, and then it reaches the maximum as shown in Fig. 11. Finally it decays slowly with time. The time in Fig. 11 is counted from the instant when the fluid front reaches the intersecting point. With increasing far-field stress σ_0^1, the magnitude of the peak fluid pressure increases, and a longer time is required for fluid pressure to reach this peak. It is interesting to note that the difference of fluid pressure in the long term is equal to the difference in the vertical far-field stress. For the case of $\sigma_0^1 = 16$ MPa, further fluid penetration into the interface is prevented after a certain amount of fluid invasion. As seen in Fig. 11, the fluid pressure at the intersecting point is still increasing at the latest time simulated. In this case, the interfacial opening near the intersection point is decreased to a very small value as displayed below. It must be mentioned that the model employed does not allow for fracture initiation in the intact side of the bedding contact. The greater fluid pressure in the parent fracture will induce larger layer-parallel

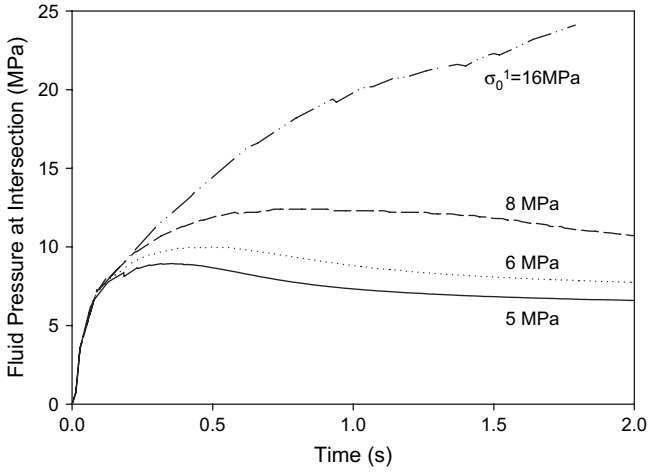

Fig. 11. Fluid pressure at the intersecting point versus time curves for various confining stresses across the interface in the case of $\mu = 0.1$ Pa s, $L = 1$ m and $\lambda = 1.0$.

tension in the intact side. This can give rise to initiation of new fracture if the tensile stress exceeds the material strength. Therefore, straight fracture growth across the interface is more likely at high confining stresses, if the frictional strength of the interface is large enough to prevent or limit slip.

The fluid length on the interface and the fluid front velocity have been plotted against time in Fig. 12 for two values of σ_0^1. Increasing the confining stress results in a decrease in the fluid front velocity post intersection since the fluid invasion into the interface becomes more difficult. But, the initial slow fluid movement is later compensated for since it is observed in Fig. 12 that the fluid velocity at $\sigma_0^1 = 8$ MPa eventually increases above that at $\sigma_0^1 = 5$ MPa. The fluid front at larger σ_0^1 will catch up with its counterpart at lower σ_0^1 since the difference in the fluid length decreases with time, as shown in Fig. 12. After a longer time, the fluid front velocity would become independent of the confining stress, as would be the case for a single channel hydraulic fracture.

To detail the responses of fluid invasion, the distributions of (a) fracture opening, (b) slip, (c) normal stress and (d) shear

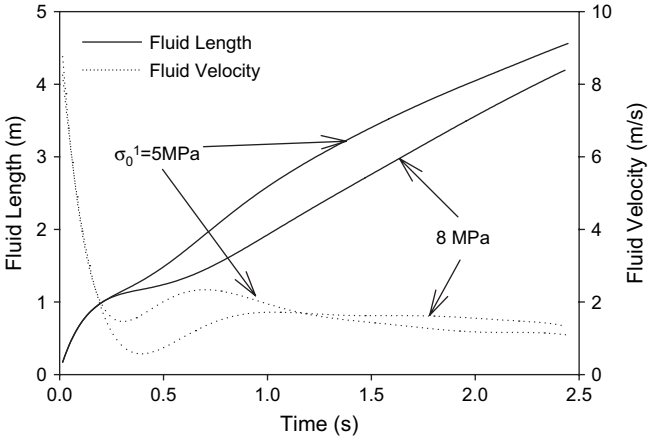

Fig. 12. Time dependence of the fluid length and fluid front velocity for two different confining stresses under the same conditions given in Fig. 11.

stress are plotted in Fig. 13 in terms of the coordinate s, for the four values of σ_0^1. The elapsed time for all cases is the same ($t = 2$ s), although $t = 1.94$ s is adopted for $\sigma_0^1 = 16$ MPa. It is found in Fig. 13(a) that the interface is closed at $s = 1$ m when σ_0^1 is increased to 16 MPa. The position $s = 1$ m corresponds to the intersecting point on the interface. On the interface ($s > 1$ m), the location with maximum opening is at some distance from the intersecting point. It is important to note that the opening at the intersecting point decreases with increasing vertical far-field stress. When $\sigma_0^1 = 16$ MPa, the pinching of the interface can impede fluid penetration. However, in this case, some parts of the interface remain opened and are filled and pressurised by previously invaded fluid. Therefore, if the vertical far-field stress is large enough, the fluid may invade the interface initially, but at a certain time during the interaction process, pinching develops and fluid invasion is blocked. The maximum opening along the parent fracture is at the intersecting point, and this opening magnitude increases with the confining stress. In addition, the extremely large opening of the parent fracture at the intersecting point for $\sigma_0^1 = 16$ MPa implies a blunted fracture. The larger fluid pressure associated with blunted fracture tip is shown in Fig. 13(c) and this can impose additional compression on the interface, leading to a pinching and hindering of further fluid invasion.

The opening profile also shows the location of the fluid front. As shown in Fig. 13(a) the fluid front at $\sigma_0^1 = 6$ MPa is very close to that at $\sigma_0^1 = 5$ MPa, and the front at $\sigma_0^1 = 8$ MPa is catching up with them because of its eventual faster fluid speed as shown in Fig. 12. This further confirms the conclusions drawn based on the findings in Fig. 12.

The maximum sliding along the bedding plane occurs always at the intersecting point as shown in Fig. 13(b) resulting from the transfer of the opening of the parent fracture into the shear displacement along the interface. The slip decreases with the distance to the intersecting point. As the vertical far-field stress is increased, the maximum slip increases as does the opening along the parent fracture. However, the size of the zone of slippage decreases. In particular, there is a small region with large slip near the intersecting point for $\sigma_0^1 = 16$ MPa, as shown in Fig. 13(b).

The normal stress drops rapidly near the ends of the opening segments on the interface, as depicted in Fig. 13(c). The normal stress is equal to the fluid pressure in the fluid-filled part and to the contact stress in the closed part. There is no dry or fluid lag region on the interface, for the numerical discretisation used, and therefore the fluid front is exactly at the fracture tip during the fracture propagation process. However, as indicated in Fig. 13(c), large stress gradients typically occur near the tip of hydraulic fractures as a result of coupled fluid flow and rock deformation. The normal stress drop identifies the high pressure gradient in the fracture channel. An increase in contact stress is found ahead of the fracture tip. The resulting pressure gradient is a driving force for fluid invasion. The small normal stress drop for $\sigma_0^1 = 16$ MPa results because of a lack of fluid flow into the interface fracture because of the restriction at the pinching point. In addition, a zone of elevated shear stress for each case exists near the fluid front

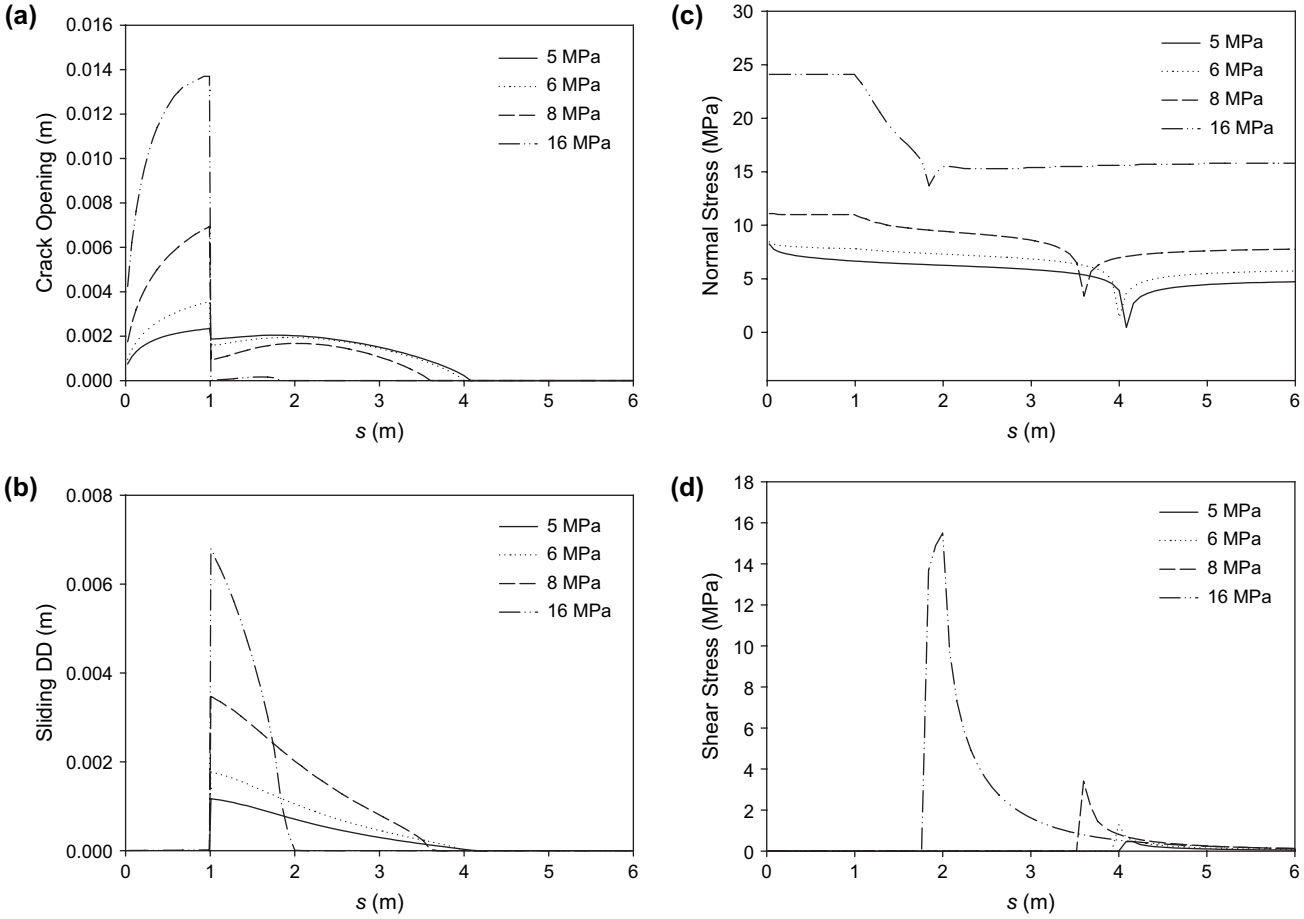

Fig. 13. Distributions of (a) opening, (b) slip, (c) normal stress and (d) shear stress for various confining stresses at $t = 2$ s, but $t = 1.94$ s for $\sigma_0^1 = 16$ MPa under the same material constants given in Fig. 11.

as shown in Fig. 13(d), which provides the resisting stress to the sliding. The shear stresses die out with the distance from the fracture front and the point of maximum shear stress coincides with the transition from sliding to sticking of the interface (failed in shear or not). The maximum shear stress reached increases with the vertical far-field stress at a given time in the simulation. The larger shear stress for $\sigma_0^1 = 16$ MPa is a reflection of the large frictional resisting strength associated with the higher confining stress.

To validate that the mechanical interaction produces the pinching on the interface at the higher confining stress, Finite Element analysis was carried out using FRANC2D (2000). The stress levels along the parent fracture and the two daughter fractures were directly extracted from the stress distribution provided in Fig. 13(c) for $\sigma_0^1 = 16$ MPa. These stresses were then imposed in FRANC2D as boundary loads. Allowing for symmetry, only half of the fracture problem is analysed. Fig. 14(b) shows the deformed mesh around the T-junction under the loading configuration as illustrated in Fig. 14(a). The interface fracture tends to be in contact at the intersecting point, but a portion of the interface is still open, as shown in Fig. 14(b). It must be mentioned that there is a small gap across the interface fracture in the original finite element mesh, so that the upper and lower surfaces of the interface at the interesting point are not touching. The opening profile on the interface is in good agreement with the result predicted by our model given in Fig. 13(a). Also, the opening along the parent fracture is much larger than that on the interface, and pinching at the intersecting point occurs. Mechanically, this pinching arises from the deformation contrast of the upper stiff rock and the lower soft one. The stiff rock in tension does not experience significant surface deformation. The rock mass around the intersecting point in the soft layer experiences a deformation pattern similar to a right-angle wedge loaded along two faces, as shown in Fig. 14(c). The compressive stresses acting on the two walls will impel the wedge corner against the surface of the upper layer to form a pinch. The formation of the pinch suggests that fluid transport along the interface will be inhibited and fracturing fluids containing solids such as proppants will not be able to penetrate this narrower region. It must be noticed that pinching depends not only on the confining stress, but also on the length of the parent fracture and other factors.

Fig. 15 shows the variations of fluid pressure at the intersecting point with time for cases considering different frictional coefficients of the interface. Similar to the fracture problems in homogeneous materials (Zhang and Jeffrey, 2006b), the coefficient of friction plays an important role in

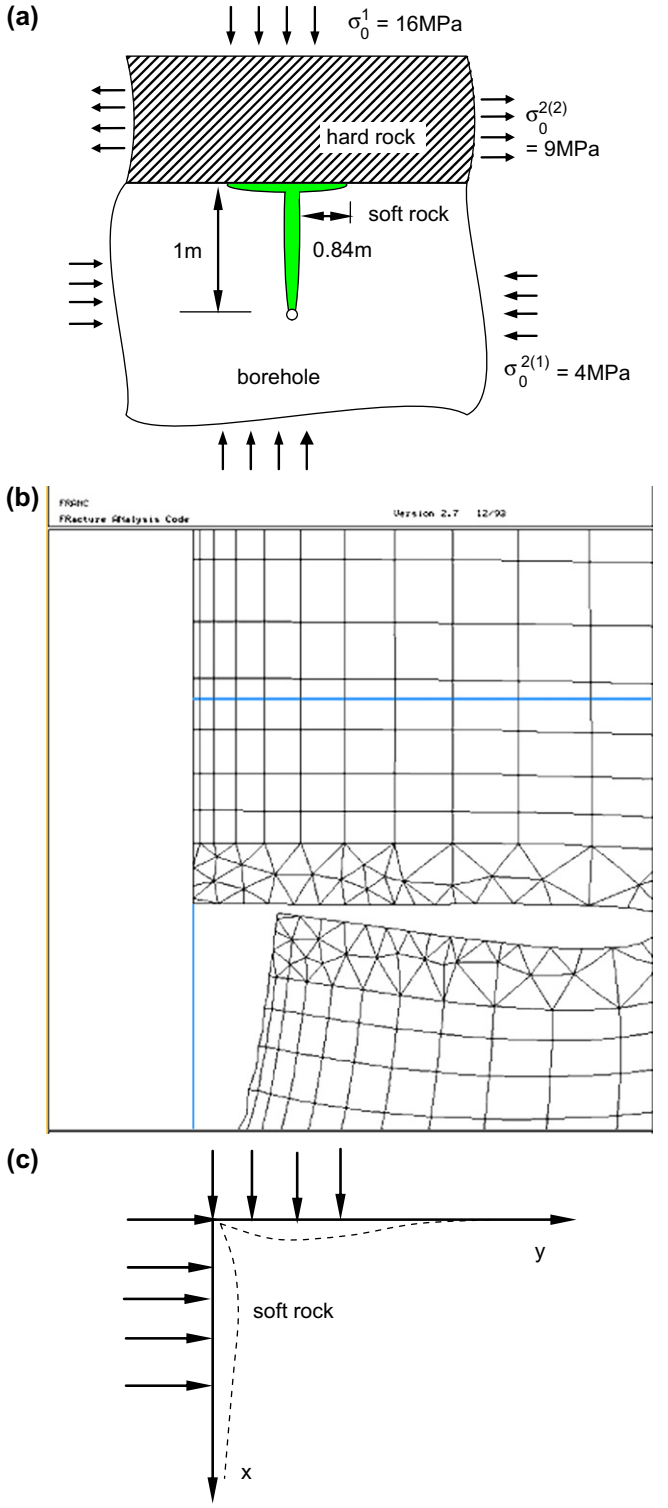

Fig. 14. (a) Fracture geometry and loading condition for interface closure at large confining stress; (b) deformed finite mesh around the T-shaped intersection from Finite Element Analysis using FRANC2D; and (c) right-angle wedge loaded along two sides and deformation profiles of both sides.

the early stage of fracture invasion. After a certain amount of fluid penetration, all curves converge to the same curve which corresponds to the solution for a fluid-driven fracture growing along a closed interface without any frictional strength or

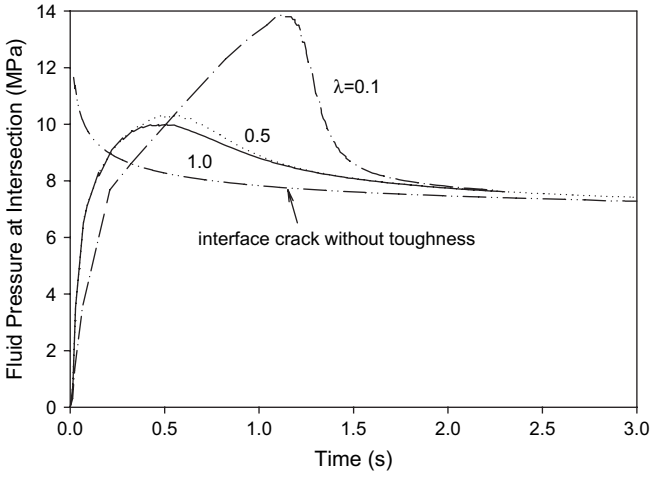

Fig. 15. Fluid pressure at the intersecting point versus time curves for various frictional coefficients ($\mu = 0.1$ Pa s, $L = 1$ m and $\sigma_0^1 = 6.0$ MPa).

adhesion, that is, the ''interface fracture'' solution. The peak pressure reached is different for various coefficients of friction. The smaller coefficient of friction results in a larger maximum fluid pressure. The interface fracture penetration is delayed for $\lambda = 0.1$ compared with the other cases since more fluid is required to generate the large fluid pressure. If the interface is frictionless, the associated large sliding would result in a fully blunted end to the parent fracture, as analysed by Zhang and Jeffrey (2006b). A low shear stress level along the interface produces relatively small tensile stress on the intact side of the interface. Therefore, it is impossible to induce new fractures in the intact layer. Instead, the parent hydraulic fracture becomes wider and wider, and is ultimately arrested at the frictionless bedding plane.

Alternatively, the reduction of fluid viscosity to a very low level or increasing it to a relatively high level will change the fracture propagation and fluid invasion process, as shown in Fig. 16. Fig. 17 displays the corresponding opening profiles at $t = 2$ s for $\mu = 0.01$ and 0.1 Pa s, as well at $t = 0.45$ s for

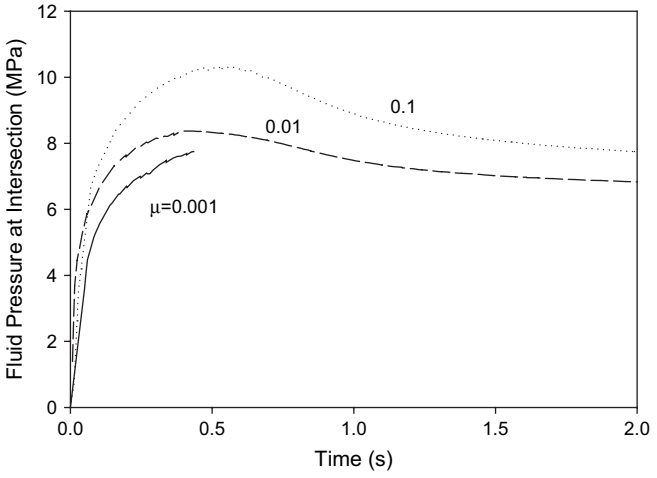

Fig. 16. Time dependence of fluid pressure at the intersecting point for various fluid viscosities ($\lambda = 0.5$, $L = 1$ m and $\sigma_0^1 = 6.0$ MPa).

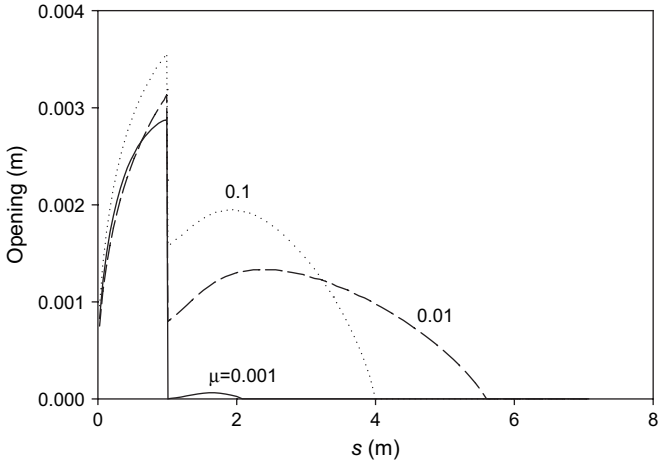

Fig. 17. Distributions of openings for various fluid viscosities at $t = 2$ s, but $t = 0.45$ s for $\mu = 0.001$ Pa s under the same material constants given in Fig. 16.

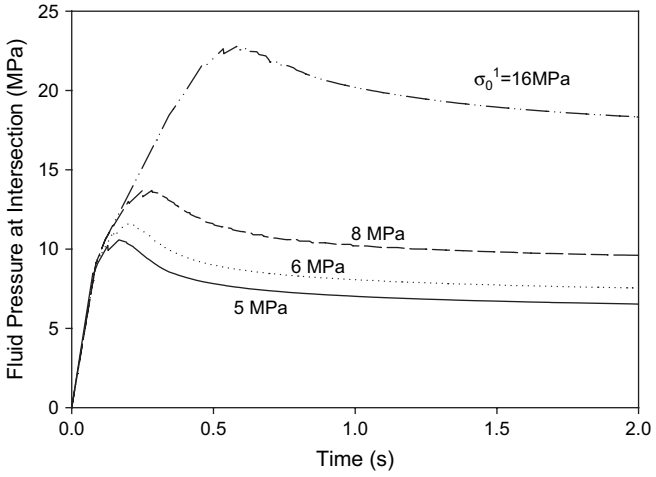

Fig. 18. Fluid pressure at the intersecting point versus time curves for various confining stresses across the interface in the case of $\mu = 0.1$ Pa s, $L = 1$ m and $\lambda = 1.0$.

$\mu = 0.001$ Pa s. The injection pressure is still rising for $\mu = 0.001$ Pa s as shown in Fig. 16, but fluid invasion along the interface is inhibited because as shown in Fig. 17, pinching develops at the intersecting point for $\mu = 0.001$ Pa s, similar to the case of large vertical far-field stress. The low-viscosity fluid can enter a small conductivity interface easily. Some fluid is trapped in an open portion of the interface as shown in Fig. 17. However, a pressure sufficient to propagate the fracture must be present before the fracture can move forwards. For the lower viscosity cases, the pressure of the fluid stored in daughter fractures is not large enough to extend the fracture tip, but it produces a loading condition similar to a deformation pattern of a right-angle wedge as shown in Fig. 13(c). This can bring about movement of the corner of the wedge, and associated pinching at the intersecting point. On the other hand, in Fig. 16, an increase in fluid viscosity can yield a higher peak fluid pressure that results in larger opening and slower fracture growth as shown in Fig. 17. In this case, more energy is consumed by the transport of high viscosity fluids. In addition, the large fluid pressure in the parent fracture can induce large tensile stress on the intact side of the bedding plane. Hydraulic fractures driven by high viscosity fluids may, for this reason, penetrate the interface, rather than deflect along the interface.

4.2. Stiff to soft

Now we look at the cases where the parent fluid-driven fracture attempts to cross the interface from the stiffer layer. In contrast to the soft-to-stiff cases, the flexibility of the soft rocks on the intact side of the interface will facilitate separation of the interface surfaces. Therefore, the tendency for pinching is not present in the cases studied. The evolution of the fluid pressure at the intersecting point is shown in Fig. 18 for various values of the vertical far-field stress. The maximum pressure increases with increasing vertical far-field stress. For the case of $\sigma_0^1 = 16$ MPa, a peak value is reached followed by a slowly decreasing pressure with time, which is associated with progressive fracture invasion along the interface.

The fracture opening profiles for different vertical far-field stresses at $t = 2$ s are given in Fig. 19. Although the fracture tip for $\sigma_0^1 = 16$ MPa has not extended as far as in the other cases, there is no pinching along the fracture path. However, there is a developing pinch near the intersecting point. A further increase in σ_0^1 may give rise to the formation of complete closure and pinching at this point. But the vertical stress required for pinching to develop is much larger than the 16 MPa value found for the soft-to-stiff cases. Compared with the curves provided in Fig. 13(a), the opening along the interface is larger and the fracture length is longer. In other words, the fracture and fluid penetration along the interface becomes easier. This indicates that the fluid-driven fractures can readily deflect into and propagate along the interface, and thus they are more likely to be terminated and become T-shaped.

Comparing the results in Fig. 18 with curves in Fig. 11 under the same stress conditions but different material arrangement,

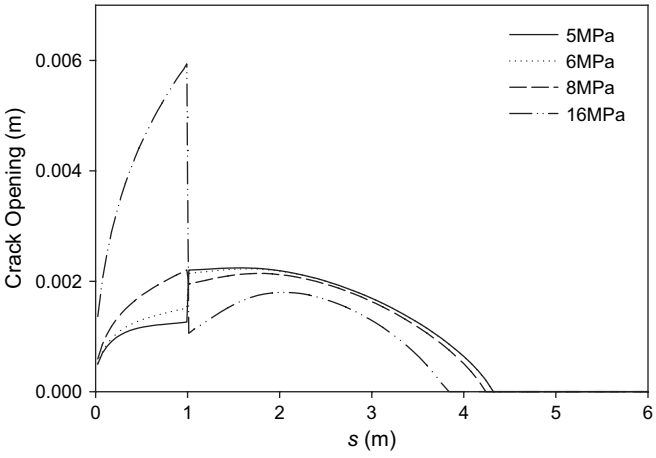

Fig. 19. Distributions of openings for various confining stresses at $t = 2$ s under the same material constants given in Fig. 18.

the peak fluid pressure is higher when the parent fracture is in the stiff layer. This is caused by the narrower channel of the parent fracture in the stiffer rock, as can be seen by the opening profiles in the parent fractures in Figs. 13(a) and 19. When the parent fracture is contained in the stiffer layer, the time interval for fluid pressure to reach the peak is much shorter than the opposite layer stiffness condition. With increasing time, all curves asymptotically approach a value that depends on the pressure needed to propagate a simple interface fracture. The plateau values reached at $t = 2$ s are 6.53, 7.52 and 9.55 for $\sigma_0^1 = 5$, 6 and 8 MPa, respectively, but the curve for $\sigma_0^1 = 16$ MPa has not reached its plateau value at $t = 2$ s. It is interesting to note that the differences in the plateau values are roughly equal to the differences in the vertical far-field stresses for these cases.

Fig. 20 demonstrates the evolution of injection pressures for different values of distances L. After the parent fracture touches the interface, the injection pressure continues to decrease. This pressure is at first lower than the "vertical fracture" solution corresponding to fluid-driven fracture growth in the stiff rock without the interface. The pressure profiles in Fig. 10 never fall below the corresponding "vertical fracture" solution. The higher modulus increases the propagation pressure before intersection with the interface, and this higher pressure facilitates fracture propagation and fluid invasion into the interface. However, the change in propagation direction is expected to result in higher pressure because of the greater confining stresses acting across the interface. Subsequently, there is a gradually increasing stage for the fluid pressure during fracture growth on the interface. Moreover, no intermediate peak of injection pressure is seen in the data of Fig. 20. The curves increase slowly to approach their plateaus as shown in Fig. 20. However, the pressure at the intersection point shown in Fig. 10 for the soft-to-stiff cases demonstrates that the injection pressure decreases with fracture growth on the interface to asymptotically approach the solution for a fluid-driven interface fracture. The increasing trend in injection pressure is attributed to the interaction of the parent and daughter fractures. Growth of the daughter fractures induces stresses that tend to squeeze and narrow the parent fracture. This, in turn, causes an increase in the local flow rate at the intersection point so that, for a period of time, it exceeds the injection rate at the borehole. The narrower parent fracture channel and the increased local flow rate both contribute to the slowly increasing pressure trend seen in Fig. 20.

The frictional properties of the interface can affect the early stage of fracture and fluid invasion, as shown in Fig. 21. Compared with the results shown in Fig. 15 for soft-to-stiff cases, the differences in the peak value for three frictional coefficients shown in Fig. 21 are much smaller, although significantly different frictional coefficients are used. It is also seen that the frictional effect can be ignored at large time since the solutions asymptotically approach the interfacial solution for a fluid-driven fracture growing on a frictionless interface. As the pure interface fracture solution is independent of material arrangement, the large-time solutions at a fixed σ_0^1 are the same for both material settings. It is noted in Fig. 21 that when the parent fracture is in the stiffer layer, the solutions after intersection approach the interfacial solutions more quickly than in the soft-to-stiff cases.

As stated above, the pinched interface profile is not found for any of the three fluid viscosities $\mu = 0.001$, 0.01, 0.1 Pa s as shown in Fig. 22. The fluid pressure at the intersecting point increases to a peak and it then decreases with time to a steady value. The slowly decreasing trend at large time can be taken as an indication of continuous fracture growth and fluid invasion along the interface. The peak value of fluid pressure at the intersecting point increases with the fluid viscosity, demonstrating that fracture penetration into the interface is easier for low-viscosity fluid cases.

5. Conclusions

A numerical method is presented to address the coupled process of rock deformation and fluid flow involved in the interaction between a fluid-driven fracture and a frictional

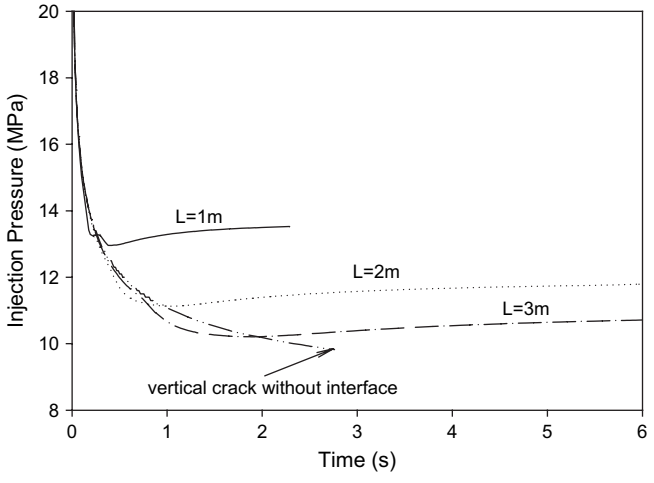

Fig. 20. Injection pressure versus time curves for various injection point distances in the case of $\mu = 0.1$ Pa s, $\sigma_0^1 = 5$ MPa and $\lambda = 1.0$.

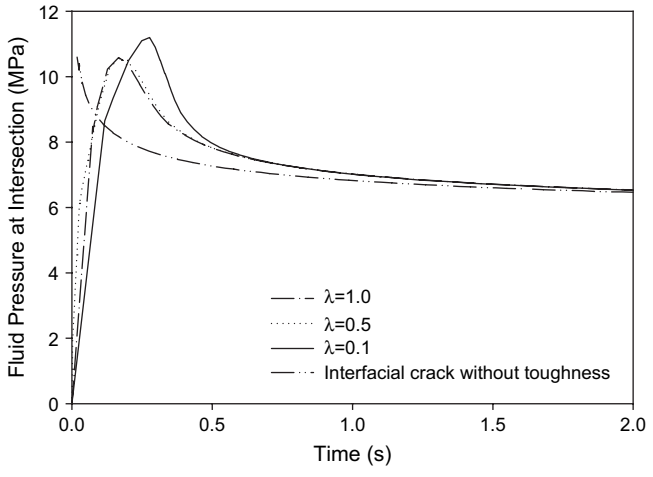

Fig. 21. Fluid pressure at the intersecting point versus time curves for various frictional coefficients ($\mu = 0.1$ Pa s, $L = 1$ m and $\sigma_0^1 = 6.0$ MPa).

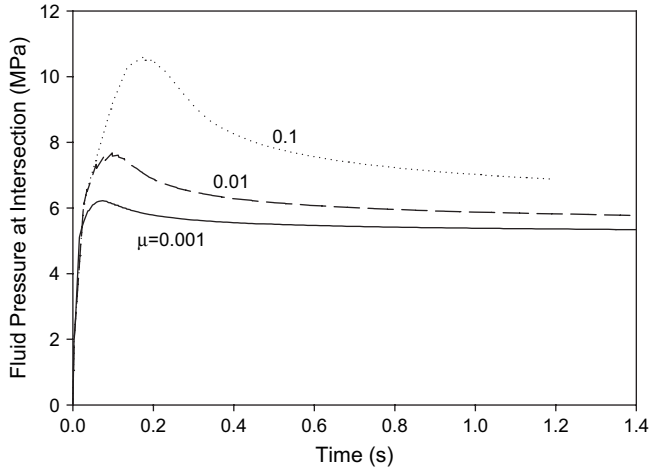

Fig. 22. Fluid pressure at the intersecting point versus time curves for various fluid viscosities ($\lambda = 0.5$, $L = 1$ m and $\sigma_0^1 = 6.0$ MPa).

interface or bedding plane. Numerical experiments have been used to explore some features of fracture deflection into and subsequent growth along the bedding contact. Various factors that affect the process, such as modulus contrast, in situ stresses, interfacial frictional strength and fluid viscosities, are considered. Hydraulic fractures propagating initially perpendicular to and towards the bedding plane can deflect into the bedding plane to create two daughter branches on the interface, post intersection. Numerical results presented show the time-dependent variations of opening, fluid pressure, contact stress and fluid front position. Previous studies from the literature contain ad hoc assumptions on stress distributions that we have relaxed, but most of their conclusions have been recovered here. In particular, fracture propagation and fluid invasion into the interface can either continue or be inhibited as a result of the local stress and deformation states at the intersecting point.

After an initially planar fracture deflects into an interface, the parent and daughter fractures interact mechanically with each other. For the case of a patient fracture originating in the soft layer of a soft-stiff pair, relatively large interface sliding associated with low frictional strength arising as a result of with low confinement or a small frictional coefficient can produce deformation that seals fluid entry into the daughter fracture at the intersecting point. This case can also result in low induced tensile stresses parallel to the interface on the intact side, making fracture re-initiation less likely. The parent fracture is therefore blunted (Zhang and Jeffrey, 2006b).

For intermediate confining stresses, the fracture driven by a lower viscosity fluid can grow into an interface with moderate frictional strength. Growth of two fracture branches occurs as the fluid volume injected increases. However, an impediment to fracture growth on the interface is associated with a peak in the time-dependent injection pressure history. The value of the peak fluid pressure increases with an increase in vertical far-field stresses and fluid viscosity, and with a reduction in the coefficient of friction of the interface and the distances to the injection borehole. The vertical far-field stress plays a two-fold role in the fracture deflection and fluid invasion along the interface. Higher vertical far-field stress can delay the fracture propagation by increasing the pressure needed for fluid invasion, but after a short time when the stress barrier is overcome, the relatively higher fluid pressure drives the fluid front faster. It is also found that the long-time solutions tend to be the same as the interface solution for a fluid-driven fracture growing along a frictionless interface. The long-time solutions are therefore independent of the frictional coefficient of the bedding plane.

The local stress states around the intersecting point resemble those around a right-angle wedge with loads exerted on both sides. The formation of a pinch point at the intersecting point occurs under the conditions of high vertical far-field stress and low fluid viscosity when the parent fracture originates in the softer layer. A small amount of fracture growth on the interface normally takes place prior to the formation of a pinch point. In these cases, high tensile stresses will build up in the intact rock on the other side of the interface opposite the parent fracture, provided the frictional strength of the interface is not too low. The higher tensile stress can result in a new fracture nucleating in the intact rock so that the hydraulic fracture can grow across the interface.

When the parent fracture is located in the stiff layer, the stress barrier on the interface for fracture invasion is weak due to the flexibility of the intact soft layer. The pinch point opening profile is not generated on the interface for the stiff-to-soft cases studied. The injection pressure initially drops below the ''vertical fracture'' solution, post intersection. Because of additional confinement on the parent fracture induced by the growth of the daughter fractures and associated squeezing of the parent fracture, a local flow rate develops at the intersection point that exceeds the injection rate specified in the parent fracture. In response, the injection pressure increases over the entire period of time simulated rather than peaking and then decreasing as it does in the soft-to-stiff case. Furthermore, the fluid-driven fracture is more likely to be terminated at the interface, rather than to reinitiate a new fracture in the intact soft rock. In addition, the long-time solutions for fracture propagation along the interface also approach the single interface fracture solution that is independent of material arrangement.

Acknowledgements

The authors thank Daniel Koehn and Xavier Maeder for their thorough review of this manuscript. This work was supported by CSIRO Division of Petroleum Resources and Schlumberger Moscow Research.

References

Baer, G., 1991. Mechanisms of dike propagation in layered rocks and in massive porous sedimentary rocks. J. Geophys. Res. 96, 11911–11929.

Becker, A., Gross, M., 1996. Mechanism for joint saturation in mechanically layered rocks: an example from southern Israel. Tectonophysics 257, 223–237.

Batchelor, G.K., 1967. An Introduction to Fluid Dynamics. Cambridge University Press, Cambridge, UK.

Cooke, M.L., Underwood, C.A., 2001. Fracture termination and step-over at bedding interfaces due to frictional slip and interface opening. J. Struct. Geol. 23, 223–238.

Crouch, S.L., Starfield, A.M., 1990. Boundary Element Method in Solid Mechanics. Unwin Hyman, Boston.

Daneshy, A., April 2003. Off-balance growth: a new concept in hydraulic fracturing. J. Petrol Technol., 78–85.

Detournay, E., 2004. Propagation regime of fluid-driven fractures in impermeable rocks. Int. J. Geomech. 4, 35–45.

Dyer, R., 1988. Using joint interaction to estimate palestress ratios. J. Struct. Geol. 10, 685–699.

Erdogan, F., Biricikoglu, V., 1973. Two bonded half planes with a fracture going through the interface. Int. J. Eng. Sci. 11, 745–766.

Fischer, M.P., Gross, M.R., Engelder, T., Greenfield, R.J., 1995. Finite-element analysis of the stress distribution around a pressurized crack in a layered elastic medium: implications for the spacing of fluid-driven joints in bedded sedimentary rock. Tectonophysics 247, 49–64.

FRANC2D. Version 2.7, 2000. Cornell Fracture Group, Cornell University, USA.

Gross, M., 1993. The origin and spacing of cross joints: examples from Montery Formation, Santa Barbara Coastline, California. J. Struct. Geol. 15, 737–751.

Gudmundsson, A., Brenner, S.L., 2001. How hydrofractures become arrested. Terra Nova 13, 456–462.

Helgeson, D.E., Aydin, A., 1991. Characteristics of joint propagation across layer interfaces in sedimentary rocks. J. Struct. Geol. 13, 897–911.

Hutchinson, J.W., Mear, M.E., Rice, J.R., 1987. Crack paralleling an interface between dissimilar materials. ASME J. Appl. Mech. 54, 823–832.

Jaeger, J.C., Cook, N.G.W., 1979. Fundamentals of Rock Mechanics. Chapman and Hall, New York.

Jeffrey, R.G., November 1996. Asymmetrically propped hydraulic fractures. SPE Prod. Facil., 244–249.

Jeffrey, R.G., Settari, A., Smith, N.P., 1995. A comparison of hydraulic fracture field experiments, including mineback geometry data, with numerical fracture model simulations. In: Proceedings of the 1995 SPE Annual Technical Conference & Exhibition, Dallas, Texas, October 22–25.

Jeffrey, R.G., Vandamme, L., Roegiers, J.-C., 1987. Mechanical interactions in branched or subparallel fractures. In: SPE 16422 Presented at the SPE/DOE Low Permeability Reservoirs Symposium, Denver, Colorado, May 18–19.

Jeffrey, R.G., Weber, C.R., Vlahovic, W., Enever, J.R., 1994. Hydraulic fracturing experiments in the great northern coal seam. In: Proceedings of the 1994 SPE Asia Pacific Oil & Gas Conference, Melbourne, November 7–10.

Keer, L.M., Chen, S.H., 1981. The intersection of a pressurized fracture with a joint. J. Geophys. Res. 86, 1032–1038.

Lam, K.Y., Cleary, M.P., 1984. Slippage and re-initiation of (hydraulic) fractures at frictional interfaces. Int. J. Numer. Anal. Methods Eng. 8, 589–604.

Lawn, B., 1993. Fracture of Brittle Materials. Cambridge University Press, New York.

Moschovidis, Z.A., Gardner, D.C., Veatch, R.W., 1994. Disposal of oily cuttings by downhole periodic fracturing injections, Valhall, North Sea: case study and modeling concepts. In: SPE 25757, SPE Drilling & Completions, December 1994, pp. 256–262.

Narr, W., Suppe, J., 1991. Joint spacing in sedimentary rocks. J. Struct. Geol. 13, 1037–1048.

Peirce, A.P., Siebrits, E., 2001. Uniform asymptotic approximations for accurate modelling of fractures in layered elastic media. Int. J. Fract. 110, 205–239.

Pine, R.J., Batchelor, A.S., 1984. Downward migration of shearing in jointed rock during hydraulic injections. Int. J. Rock Mech. Min. Sci. Geomech. 21 (5), 249–263 (abstract).

Pollard, D.D., Aydin, A., 1988. Progress in understanding joints over the last century. Geol. Soc. Am. Bull. 100, 1181–1204.

Price, N.J., Cosgrove, J.W., 1990. Analysis of Geological Structures. Cambridge University Press.

Rubin, A.M., 1995. Propagation of magma-filled fractures. Annu. Rev. Earth. Planet. Sci. 23, 287–336.

Thiercelin, M. Roegiers, J.C., Boone, T.J., Ingraffea, A.R., 1987. An investigation of the material parameters that govern the behavior of fractures approaching rock interfaces. In: Sixth International Congress of Rock Mechanics, pp. 263–269.

Tuhkuri, J., 1997. Dual boundary element analysis of closed fractures. Int. J. Numer. Methods Eng. 40, 2995–3014.

Van As, A., Jeffrey, R.G., 2000. Caving induced by hydraulic fracturing at Northparkes Mines. In: Girard, J., et al. (Eds.), Pacific Rocks 2000: Proceedings of the Fourth North American Rock Mechanics Symposium, July 31–Aug 3, 2000, Seattle, Washington. A.A. Balkema, Rotterdam, The Netherlands, pp. 353–360.

Warpinski, N.R., Teufel, L.W., 1987. Influence of geologic discontinuities on hydraulic fracture propagation. J. Petrol. Technol., 209–220.

Weertman, J., 1980. The stopping of a rising, liquid-filled fracture in the earth's crust by a freely slipping horizontal joint. J. Geophys. Res. 85, 967–976.

Zhang, X., Detournay, E., Jeffrey, R., 2002. Propagation of a penny-shaped hydraulic fracture parallel to the free-surface of an elastic half-space. Int. J. Fract. 115, 125–158.

Zhang, X., Jeffrey, R.G., Detournay, E., 2005. Propagation of a fluid-driven fracture parallel to the free surface of an elastic half plane. Int. J. Numer. Anal. Methods Geomech. 29, 1317–1340.

Zhang, X., Jeffrey, R.G., 2006a. Numerical studies on fracture problems in three-layered elastic media using an image method. Int. J. Fract. 139, 477–493.

Zhang, X., Jeffrey, R.G., 2006b. The role of friction and secondary flaws on deflection and re-initiation of hydraulic fractures at orthogonal pre-existing fractures. Geophys. J. Int. 166, 1454–1465.